ACS OMEGA

http://pubs.acs.org/journal/acsodf

Article

Enhanced Photocatalytic Degradation with Sustainable CaO Nanorods Doped with Ce and Cellulose Nanocrystals: In Silico Molecular Docking Studies

Muhammad Ikram,* Ayesha Khalid, Anum Shahzadi, Ali Haider, Sadia Naz, Misbah Naz, Iram Shahzadi, Anwar Ul-Hamid,* Junaid Haider, Walid Nabgan,* and Alvina Rafiq Butt

Cite This: *ACS Omega* 2022, 7, 27503−27515

Read Online

ACCESS | Metrics & More | Article Recommendations | Supporting Information

ABSTRACT: This research work intends to evaluate the photoactivity of calcium oxide (CaO) nanorods (NRs) doped with cellulose nanocrystals (CNCs) and cerium (Ce). CNC-doped CaO and Ce/CNC codoped CaO were synthesized via the sol−gel technique. Structural, optical, morphological, physiochemical, phase constitution, and functional group evaluations were performed. The photodegradation of the prepared nanostructures was analyzed by observing photodegradation of a mixture of methylene blue and ciprofloxacin dye under light irradiation. The photocatalytic activity of the dye was drastically enhanced upon codoping in CaO. For both *Escherichia coli* and *Staphylococcus aureus*, statistically significant inhibitory zones ($p < 0.05$) were achieved in the case of CNCs and pristine and codoped CaO. Furthermore, in silico molecular docking studies (MDS) were accomplished against DNA gyrase from nucleic acid biosynthesis and enoyl-[acyl-carrier-protein] reductase (FabI) from the fatty acid biosynthetic pathway to rationalize the possible mechanism behind these antibacterial activities.

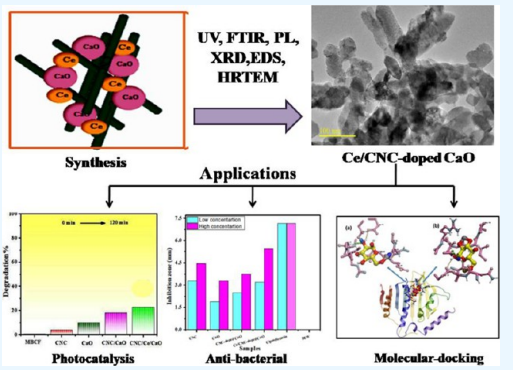

1. INTRODUCTION

Recently, the remarkable increase in water pollution caused by dye emission from various industries such as paper and fabric manufacturing and processing as well as paint and makeup manufacturing has been identified as a significant concern. The emergence of this menace will have negative effects on freshwater ecosystems. The current worldwide research of the colorant industry for 2021 predicts that the market will grow from its present value of 32 billion USD to 42 billion USD. Every year, 700,000 tons of synthetic dyes are generated, with 15% of colors released into water being hazardous or xenobiotic in nature.[1,2] Photosynthesis is inhibited by the presence of dyes in water, which also restricts the microbiological activity of aquatic plants.[3] Coagulation, membrane separation, adsorption, microbial degradation, photochemical, and filtration techniques have all been employed to remove dye effluents from wastewater.[4,5] The major source of worry is the development of harmful byproducts as a result of the design to adopt these approaches for wastewater cleanup.[6,7] Hence, the main concern is generating eco-friendly byproducts in photocatalysis. Photogenerated electrons (CB) and holes (VB) in the photocatalyst initiate redox reactions. These compounds are desorbed from the surface and are reintroduced into the fluid phase.[8,9]

Advanced oxidation processes have increased the curiosity for complete degradation of dyes, which include processes like photocatalysis, photo-Fenton, and photo-ozonation.[10,11] The medium for the reaction and atmospheric conditions, catalyst properties, band gap (E_g), surface charge, nature of the reaction medium, and environmental conditions affect the efficiency of advanced oxidation processes.[12,13] Extensively, for the degradation of dyes, a variety of photocatalysts such as metals, metal oxides, semiconductors, and so forth are under study in wastewater treatments.[14,15] Recently, researchers have concentrated on combining inorganic materials with conductive polymers to realize interactive and compatible behaviors for increasing the pollutant's degradation rate.[16,17] For this purpose, metal oxide nanoparticles (NPs) have been widely applicable to degrade nonbiodegradable dyes using the photocatalytic process.

In this document, for effective dye degradation, codoped calcium oxide (CaO) NPs have been used as photocatalysts.[18] In general, CaO white, caustic, alkaline, and crystalline powder are used. CaO has the highest $E_g \sim 4.17$ eV and a dielectric

Received: May 3, 2022
Accepted: July 14, 2022
Published: July 26, 2022

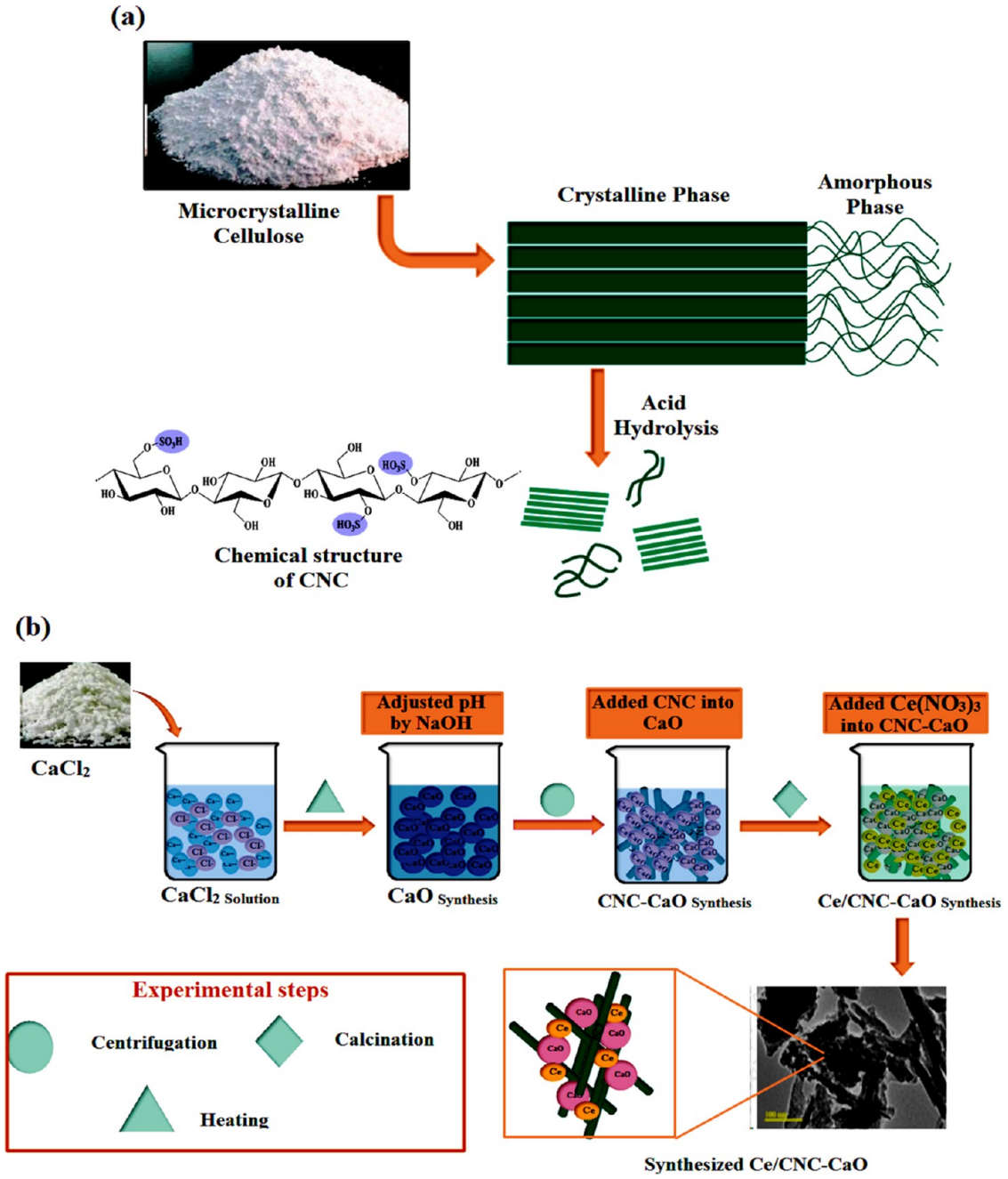

Figure 1. (a) Cellulose nanocrystal synthesis; (b) schematic of the synthesis of Ce/CNC-doped CaO nanostructures.

constant of 11.8 among light alkaline earth oxides.[19] CaO is applied in many fields, which includes its use as additives in refractory, bactericides in the biomedical field, and adsorbents especially in catalysis.[20] For photocatalytic dye degradation, however, developing high-performance CaO that provides more active sites and a large specific surface area is still a challenge. Nano-photocatalysts containing rich surface states, large surface area, and characteristic morphology are novel materials.[21] However, lower efficiency and formation of secondary pollutants result when nano-photocatalysts agglomerate during the reaction, which limit their development and usage.[22] Therefore, to overcome these challenges, semiconductor NPs coupled by a matrix produce a semiconductor/matrix composite.[23] CaO was doped with cellulose to enrich the photocatalytic activity. Cellulose is an ideal matrix with high hydrophilic character, transparency, physiochemical resistance, permeability, flexibility, and thermal stability.[24] Cellulose, which is a natural polymer, is commonly employed in polymer nanocomposites synthesis because of its abundance and biodegradability.[25] Good environmental stability cellulose is highly favored as it is preferred for synthesizing composites, providing an interface for charge transfer and also decreases leakage of ions.[26,27] Cellulosic materials have superior mechanical capabilities, are cost-beneficial, have a lower density, and have tunable surface features.[28,29] Generally, CNCs are produced with concentrated H_2SO_4 through the acid hydrolysis method.[30,31] Cellulosic nanostructures are acknowledged as unique nanomaterials that can create new high-performance materials.[32,33] Cellulose is a polymer as one unit of cellulose has three hydroxyl groups, and

https://doi.org/10.1021/acsomega.2c02732
ACS Omega 2022, 7, 27503−27515

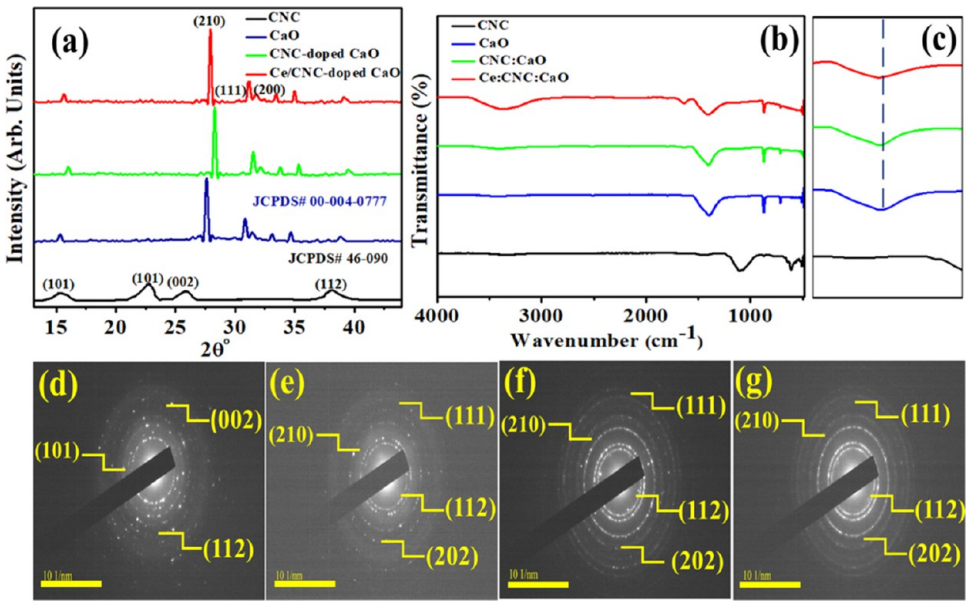

Figure 2. (a) XRD spectra, (b) FTIR profiles of codoped CaO, (c) zoom FTIR profile of products, (d–g) SAED profiles of CNC, CaO, CNC-doped CaO, and Ce/CNC-doped CaO, respectively.

the polymer is connected by β-1-4 glucosidic bonds.[34,35] Hydrogen connections established between the hydroxyl groups in the cellulose molecules allow the molecules to create a highly organized crystal structure. As a result, cellulose possesses a high degree of crystallinity.[36] The hydroxyl group of cellulose has a strong electron providing effect and a low electron loss tendency because of the lone electron pair of oxygen atoms.[37,38] In this perspective, CNCs may be the most viable alternative for fabricating cellulosic materials for new uses.[39,40] Lanthanide ions have been considered as innovative dopants to affect the structural and optoelectronic characteristics of CaO.[41] By forming complexes with various Lewis bases, it is possible to increase the absorbability of organic contaminants on metal surfaces. Among these, cerium doping attracted more interest; in redox conditions, cerium oxide shifts between CeO_2 and Ce_2O_3 because of the redox couple Ce^{+3}/Ce^{+4}. Different optical and catalytic properties result from different electronic structures between Ce^{3+} ($4f^1\ 5d^0$) and Ce^{4+} ($4f^0\ 5d^0$).[42] Ce doping on CaO plays a key role as it increases defects in surface layers in photocatalytic activity. Thus, this research attempts to enhance the photocatalytic activity of codoped CaO in degradation of MBCF under visible light. As far as we know, the production of CNC/Ce-doped CaO and its utilization in organic pollutant degradation and antibacterial activities have been unfamiliar.

Therefore, binary dopants (CNC and Ce) doped into CaO synthesized with sol–gel and examine the effect of dopants for dye degradation and antibacterial activity. Furthermore, antibacterial properties of the produced nanocomposites have been investigated using in silico MDS on enzymes from the nucleic acid and fatty acid biosynthesis pathways.

2. EXPERIMENTAL DETAILS

2.1. Materials. Calcium chloride dihydrate (99.9%), sodium hydroxide (99%), cerium nitrate hexahydrate (99%), methylene blue, and avicel $(C_6H_{10}O_5)_n$ were procured from Sigma Aldrich. The experiments involve bacterial growth media to perform bactericidal activities.

2.2. Preparation of CNC. Sulfuric acid hydrolysis of microcrystalline cellulose (Avicel) provided CNC (Figure 1a). First, avicel was hydrolyzed in H_2SO_4 (64% w/w) at 45 °C for half an hour. After that, DI water was added to suppress the reaction. The obtained cellulose pallet in the solution was centrifuged at 6000 rpm for 10 min. The Buchner flask and funnel were used to wash it, and sodium hydroxide 0.25 mol/L was added to the suspension for neutralization. Finally, the remaining suspension was sonicated for 5 min with a vibrance sonicator.[43]

2.3. Preparation of (CNC-Doped CaO) and (Ce/CNC-Doped CaO). Chemical precipitation was adopted to prepare metal oxide (CaO) nanoparticles. Supersaturated solution of CaO nanoparticles was obtained by adding NaOH in $CaCl_2$ under continuous stirring at 100 °C for 40 min. To obtain uniformly sized nanoparticles, the solution was kept static. $Ca(OH)_2$ was washed several times with DI water and centrifuged at 7100 rpm for 9 min. The achieved pallet was dried at 70 °C for 24 h, and the powder was obtained. The same method was reprised by methodically adding 2% Ce and 2.5 mL of CNC to obtain CNC-doped CaO and Ce/CNC-doped CaO nanostructures, as illustrated in Figure 1b.

2.4. Absorption and Photocatalytic Activity Process. Photocatalytic reduction of MBCF (10 mg/L) was observed in accordance to the photocatalysis of Ce-doped and Ce/CNC-doped CaO nanorods. To gain equilibrium between dye and Ce/CNC-doped CaO, 10 mg photocatalyst suspension in 60 mL MBCF was prepared. In the absorption method/procedure, the prepared solution was vigorously stirred at 50 rpm in dark conditions for 5 min before illumination. During photocatalysis, a Hg lamp (400 W, $\lambda \sim 400$–700 nm) was employed as a source of visible light. A suspension (5 mL) was obtained for UV–Vis absorption to determine the concentration of MBCF under visible light for specific time intervals. During the photocatalytic activity, decolorization was represented by a function of absorption peak intensity (665 nm) with irradiation time. The percentage age deterioration was calculated using eq 1:

https://doi.org/10.1021/acsomega.2c02732
ACS Omega 2022, 7, 27503–27515

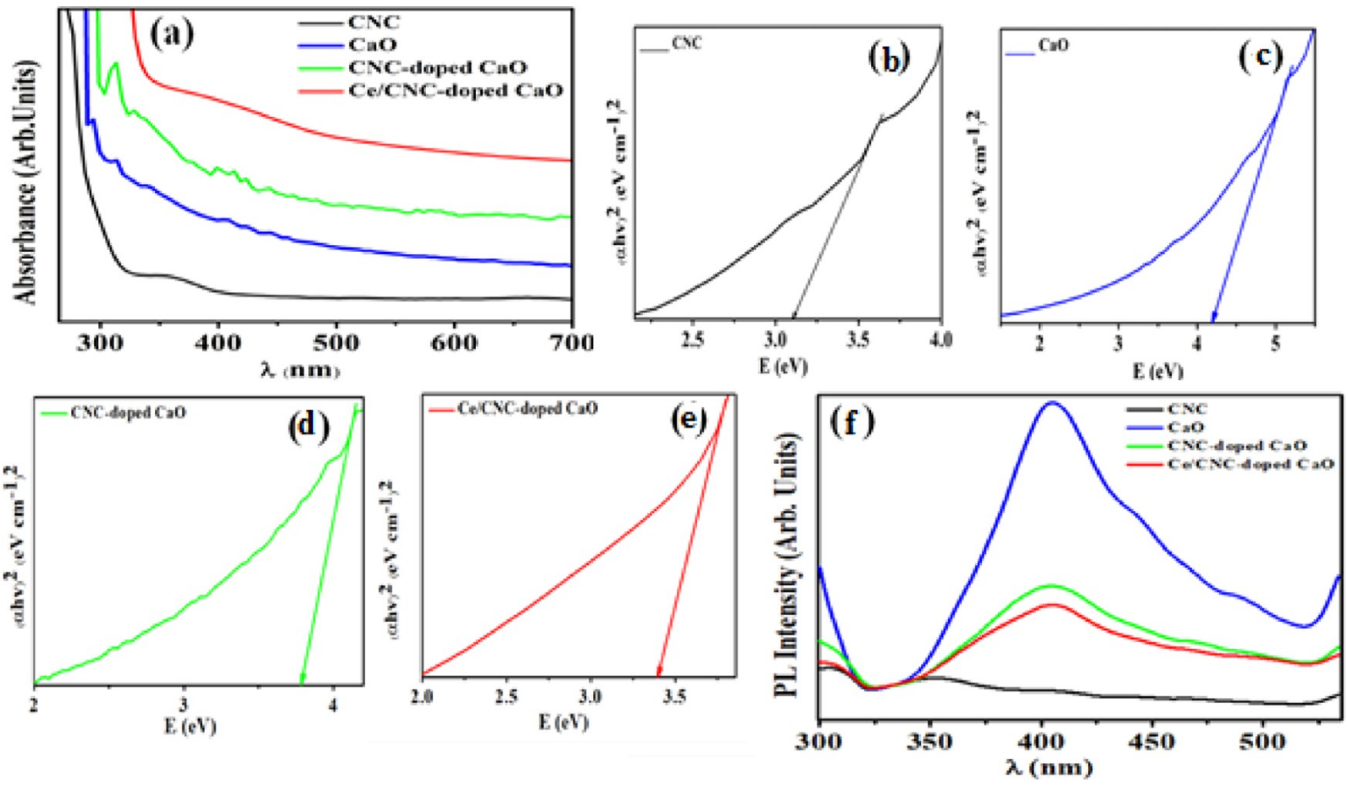

Figure 3. (a) Absorption spectra and (b) PL spectra; (c–f) Tauc plot for the band gap.

$$\%\text{degradation} = \frac{(C_0 - C)}{C_0} \times 100 \quad (1)$$

where C_0 and C are the starting and final MBCF solution concentrations following a set irradiation duration at 665 nm.

3. RESULTS AND DISCUSSION

The crystalline material structures of CNC, CaO, CNC-doped CaO, and Ce/CNC-doped CaO were inspected via X-ray diffraction (XRD) (Figure 2a). The diffractogram of CNC perceived peaks at 12°, 19.5°, 22.4°, and 33.9° that are attributed to (101), (002), and (112) crystal planes, which confirmed the monoclinic structure well harmonized with JCPDS card No. 46-090.[39] Peaks located at ∼28.53°, 32.2°, 37.3°, and 47.306° corresponding to (210), (111), (200), and (112) planes for undoped (CaO) and codoped CaO. In accordance with JCPDS card No. 00-004-0777, it demonstrated a cubic structure without impurities.[20,27,44,45] In the XRD pattern of CaO, a few low-intensity calcite peaks ($CaCO_3$) illustrate rapid carbonation of CaO by atmospheric CO_2.[46] Upon codoping, the slightly shifted layer spacing to higher values is attributed to the homogeneous distribution of Ce and CNC between interlayers of pure CaO, which is consistent with the peak shift observed in XRD spectra. With Ce and CNC addition, no obvious peak and crystal phase of dopants was noticed in XRD spectra, implying that dopants are homogenously distributed in the CaO matrix and their concentrations are too low for detection. Ce-related compounds are not developed during the growth, but the atoms of Ce are incorporated in CaO lattice sites. Crystallite sizes of CNC, CaO, CNC-doped CaO, and Ce/CNC-doped CaO were determined as ∼10.11, 11, 12.3, and 13.1 nm, respectively, using the Debye–Scherer equation. To analyze attached functional and molecular vibration modes in samples, the Fourier transform infrared (FTIR) technique was utilized (Figure 2b, c zoom). The observed spectra for CNC exhibited a transmittance band at 1082 cm^{-1}ascribed to C–O vibrations. In contrast, the peaks detected around 1635 and 1435 cm^{-1} are related to C=O stretching vibrations and C–H stretching vibrations, respectively.[47] It was revealed that the CaO band at 3647 cm^{-1}, which was attributed to the O–H bonds, was expressed by the presence of –OH and H_2O on the samples' external surface when handling the samples to record their spectra.[46] Carbonation of CaO nanoparticles indicated broad bands around 1400–1500 cm^{-1} endorsed to the C–O bond. The asymmetric stretching vibration of C=O from carbonate groups is shown by band widening with weak intensity at 1388.42 cm^{-1}.[48] The sharp peaks found that ∼874 and 712 cm^{-1} are ascribed to Ca–O–Ca and Ca–O bonding, respectively, identified the presence of CaO.[49] Because of constant active phase amounts, no notable change in intensity was observed. A slight shift toward a higher wavenumber was also observed upon Ce/CNC doping in the CaO lattice.

The selected area electron diffraction (SAED) analysis of the pristine and Ce- and CNC-doped materials revealed distinct rings that correspond to the *hkl* values (planes) of NPs, as illustrated in Figure 2d–g. These results are attributed to well-crystallized specimens, and ring indexing is supported by previous with XRD results.

The obtained absorption spectra of pristine and doped CaO with a UV–vis spectrophotometer are depicted in Figure 3a. The absorption band for CNC has been measured at 340–390 nm, depicting 3.15 eV band gap.[50] The absorbance of CaO was observed between 290 and 340 nm. Upon doping of Ce and CNC, the absorption increased and introduced red shift. E_g of samples decreased from 4.17 eV (CaO) to 3.41 eV (Ce/CNC-doped CaO), as shown in the tauc plot (Figure 3b–e). Calculated E_g values for pure CaO (4.17 eV) and CNC (3.15

https://doi.org/10.1021/acsomega.2c02732
ACS Omega 2022, 7, 27503–27515

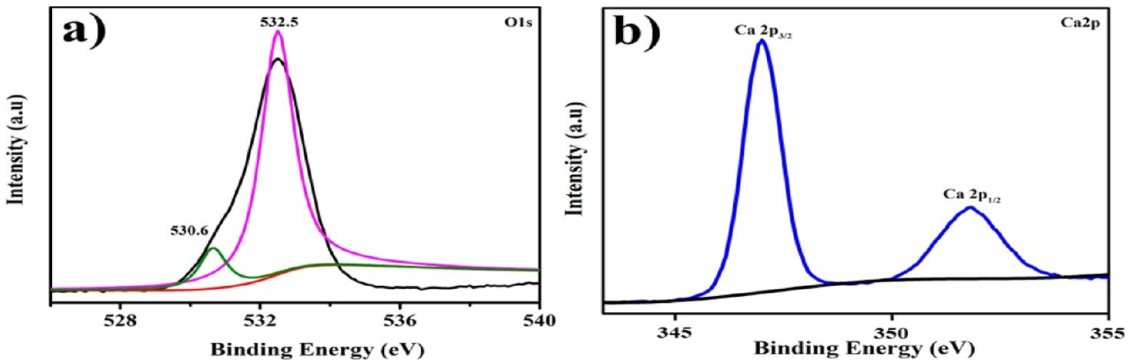

Figure 4. XPS spectra of CaO (a) O 1s and (b) Ca 2p.

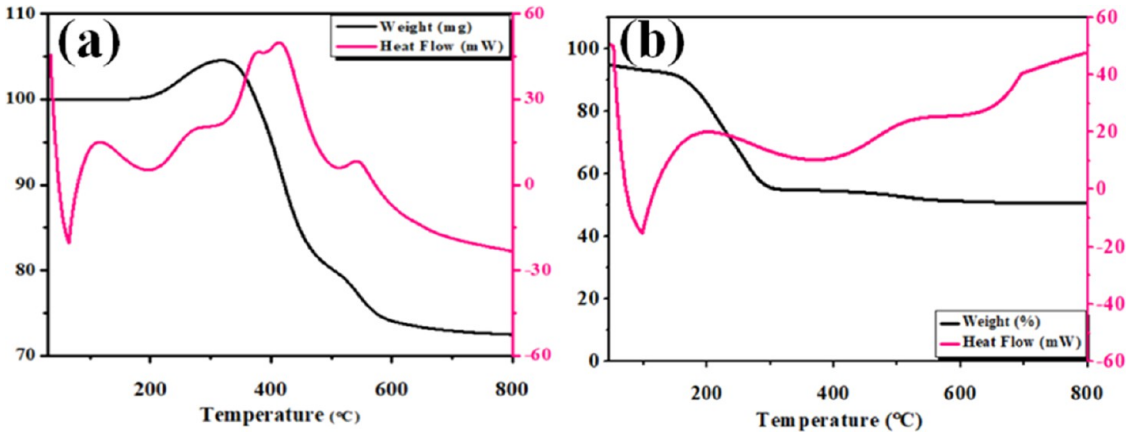

Figure 5. TGA curves of (a) CaO and (b) CNC-doped CaO.

eV) were in good agreement with the reported results.[20,51] The redshift in absorption edges for nanorods arises from the quantum size effect and is considered mandatory for enhancement in photocatalytic behavior.[52]

To analyze the trapping efficiency, electron−hole recombination, and charge carrier transportation of the synthesized product, PL was employed. The significance of Ce/CNC in promoting electron transfer and PL emission spectra of pristine and codoped CaO was measured from 400 to 700 nm (Figure 3f). Because PL emission is associated with the surface states, oxygen sites and defects are produced on the sample surface. CNC is characterized by the emission band located in the 325−700 nm region under excitation at 300 nm.[26] In the red region with the exception of photoluminescent CaO bands shifted to the infrared (IR) region to a lesser range of the band in the red region, $Ca(OH)_2$ is denser than cubic CaO and has a lower energy interface defect.[53] Band to band transition raised spontaneous emission at the PL emission peak (400 nm). The catalytic activity of CaO was enhanced by unsaturated surface sites, and photoluminescence spectra are formed by unsaturated sites on the CaO surface.[54] Surface unsaturated sites with the coordination number <5 was exhibited by the lower energy region.[55] In low coordination states, surface absorption bands connected with electronic transitions in surface oxygen ions display low PL energy excitation. Surface absorption bands are linked with the electronic transitions in surface oxygen ions in the low coordination state, which causes lower excitation energy of PL.[56] PL intensity decreased as excited electrons jumped from VB to the new state introduced by doping.

The various electronic states of CaO have been investigated by XPS, as clarified in Figure 4a, b. The signal at 532.5 and 530.6 eV, corresponding to O^{2-} and O^{1-} in Ca−O interactions, was equally detected in O 1s spectra; Figure 4 (a). Two specific heights at 346.5 and 351.2 eV found were ascribed to Ca $2p_{3/2}$ and Ca $2p_{1/2}$ in CaO, as shown in Figure 4b.[57]

These thermogravimetric analysis curves for CaO and CNC-doped CaO have been recorded in air and are depicted in Figure 5a, b. Using a 10 °C min^{-1} ramp rate, the sample was heated from ambient temperature to 800 °C. It is believed that the oxidation of CaO results in an increase in mass up to 420 °C, a process known as an exothermic reaction. This initial mass loss is caused by the breakdown of $Ca(OH)_2$ in the CaO sample; in turn, this decomposition of $Ca(OH)_2$ results from the interaction of CaO with water, which produces $Ca(OH)_2$. It has been discovered that dehydration occurs first and results in the elimination of water from crystallization about 100 °C, but a hump detected around 200 °C indicates that the transition is endothermic in nature. When the temperature is increased to 420 °C, an endothermic peak is detected, indicating that CaO melts without any associated mass loss.[58,59]

The morphology and crystal structure at single grain's edges of nanoparticles and individual atomic plane periodic arrangement in samples was observed by high-resolution transmission electron spectroscopy (HR-TEM). Figure 6a′−d′ exhibits HR-TEM images of CNC, CaO, CNC-doped CaO, and Ce/CNC-doped CaO, respectively, along with the corresponding TEM images (Figure 6a−d) with marked lattice fringes. The HR-TEM micrograph revealed that CaO has agglomerated a nanocrystalline structure with an inhomogeneous spherical shape (Figure 6b′). Nanoparticles slightly scattered with slight

https://doi.org/10.1021/acsomega.2c02732
ACS Omega 2022, 7, 27503−27515

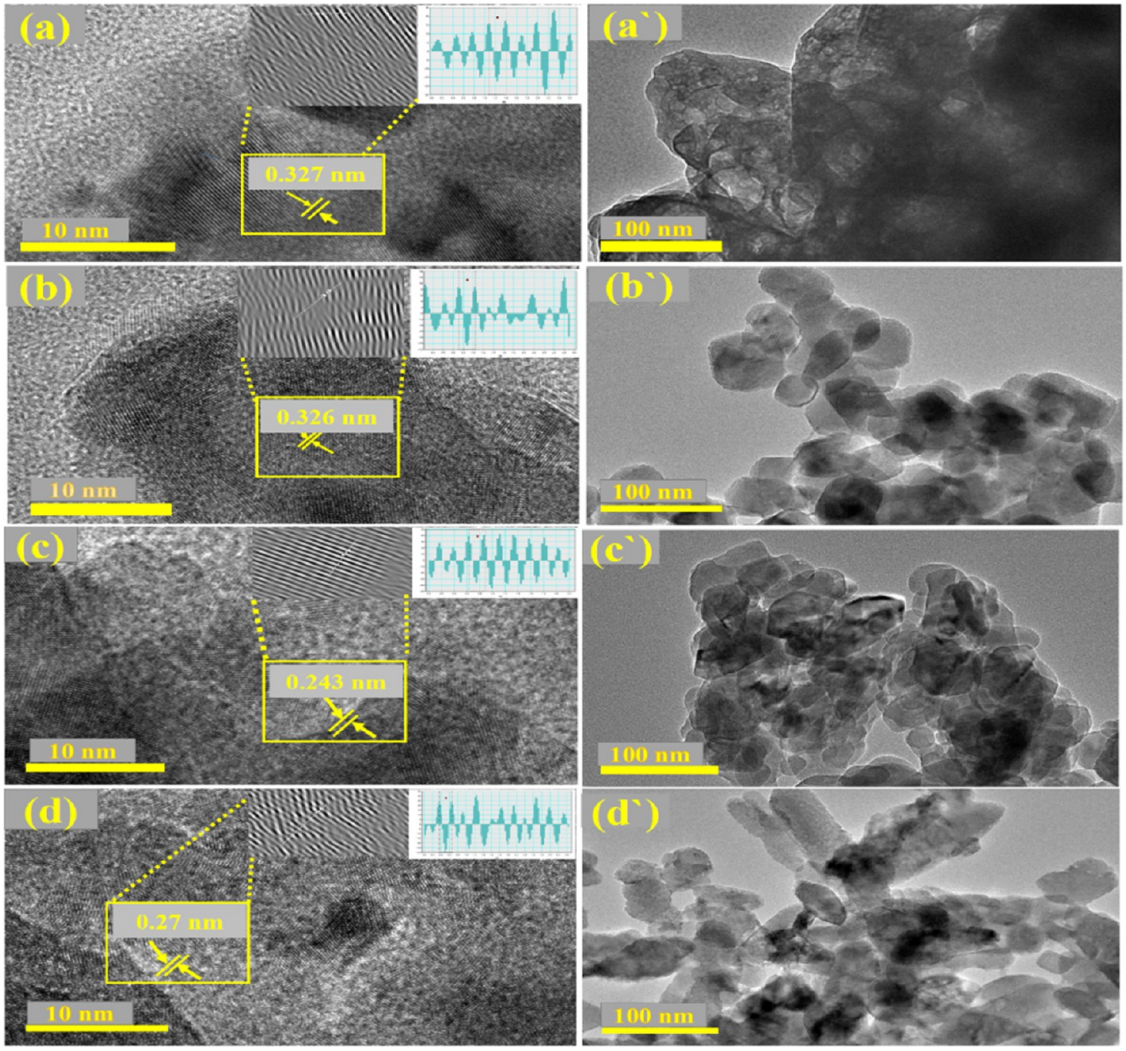

Figure 6. (a−d) *d*-Spacing calculated using HR-TEM images of CNC (a′), CaO (b′), CNC-doped CaO (c′), and Ce/CNC-doped CaO (d′). HR-TEM scale bar is 100 nm.

transparency with agglomeration and random rationing when doped with CNC and Ce (Figure 6c′,d′).The clearer image of CNC is shown in Figure S6, which indicates the nanocrystalline nature of cellulose. Ce/CNC-doped CaO depicted the formation of nanorods with agglomeration (Figure 6d′). These rod-like structures manifested increased photocatalytic activity by contributing a large surface area and a greater number of active sites. Furthermore, HR-TEM micrographs up to 10 nm resolution were recorded to acquire details about the interplanar distance and morphology of samples, as represented in Figure 6a−d. The calculated interplanar *d*-spacing values came out to be ∼0.327, 0.326, 0.240, and 0.250 nm for CNC, CaO, CNC-doped CaO, Ce/CNC-doped CaO, respectively, computed using Gatan Digital Micrograph (GDM) software and ascribed to a *hkl* planes set (210), (112), and (202), well harmonized with corresponding diffraction patterns attained from XRD results consistent with (JCPDS card No. 46-090 for CNC &JCPDS card No. 00-004-0777 for CaO).

Energy dispersive X-ray (EDX) spectroscopy was carried out to analyze the sample's elemental composition, as expressed in Figure 7a−d. The obtained images show strong peaks of Ca, O, and C, which confirmed the formation of codoped CaO nanorods. Atomic ratios (1:1) of Ca and O elements were quantified by EDX data, which are approximately near stoichiometric analysis of CaO. From the test results of doped samples, dopants (CNC and Ce) manifested in all samples as per concentrations of dopants.

Photocatalysis was enhanced by the defect addition because of dopants, leading to narrowing of E_g by structural changes. By the decomposition of dye (MBCF), the photocatalytic activity of CNC, CaO, CNC-doped CaO, and Ce/CNC-doped CaO was examined after desorption or adsorption under irradiation attained in the dark for 10 min. The sample has been exposed to visible light irradiation, and a 3 mL volume of dye was syringed out at certain intervals of time for UV−Vis analysis. When the dye concentration was reduced, it was discovered that the absorbance maxima at 665 nm were reduced as a result. The graph between MBCF concentrations (C/C_o) as a function of irradiation time evaluated the photodecolorization activity, as presented in Figure 8a. Furthermore, kinetics of photodegradation were analyzed using pseudo-first-order, and rate constants were calculated for CNC, CaO, CNC-doped CaO, and Ce/CNC-doped CaO as 0.00332, 0.00236, 0.00292, and 0.00258 min^{-1}, respectively (Figure 8b). The recombination rate of electron−hole pairs reduces by

https://doi.org/10.1021/acsomega.2c02732
ACS Omega 2022, 7, 27503−27515

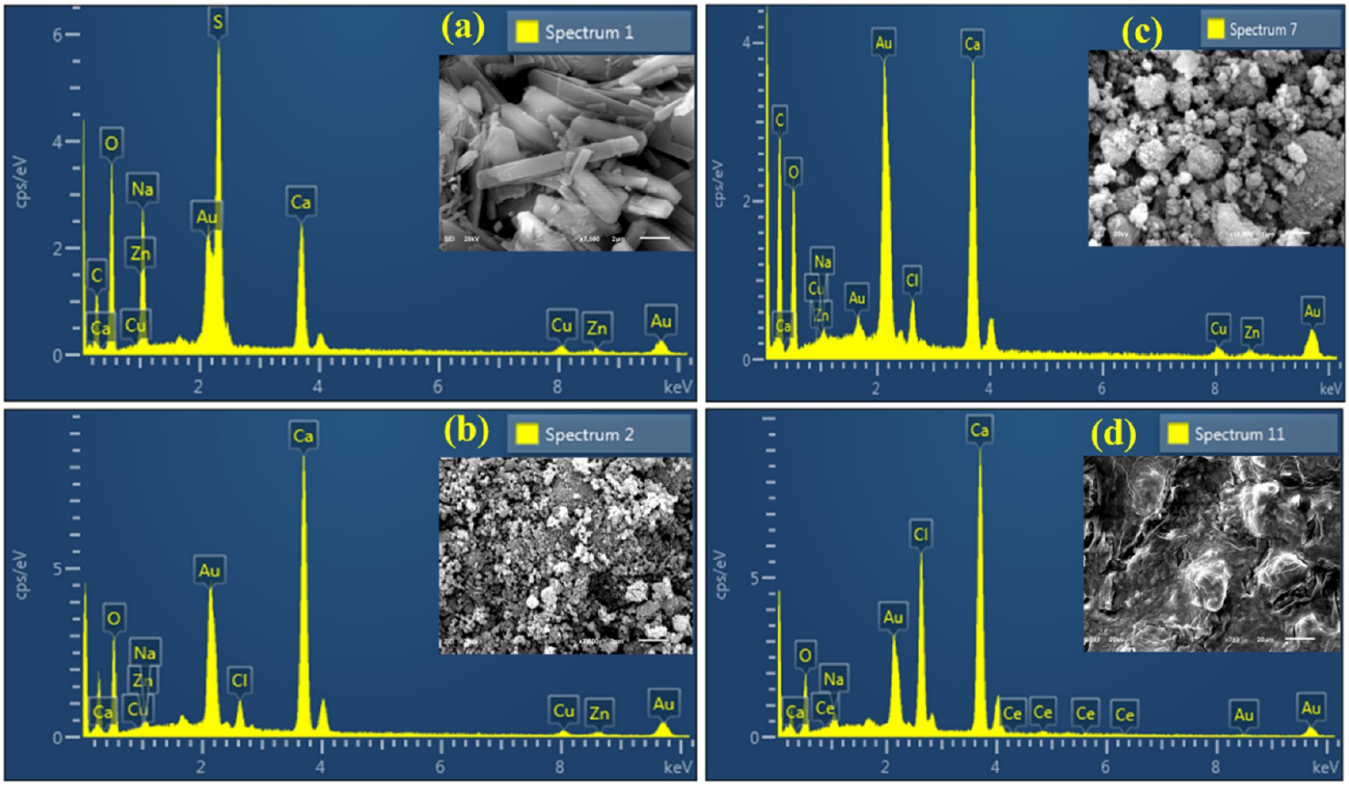

Figure 7. EDS analysis of CNC (a), CaO (b), CNC-doped CaO (c), and Ce/CNC-doped CaO (d).

intermediate energy levels because of the addition of Ce/CNC dopants, so rate constants and dye photodegradation values of codoped CaO were evaluated to be better than dopant-free CaO. Degradation largely depends on surface area, size, shape, and absorption behavior on different surfaces of the nanocatalysts. The larger the surface area of the particles, the higher the number of active sites for atoms, which in turn leads to an increase in redox reaction, which in turn causes the dye to degrade. Experiment stability is a critical factor to be considered while utilizing as a photocatalyst for wastewater treatment. CNC and all samples of CaO (pristine and doped) degraded MBCF within 120 min, while pure CaO showed the lowest degradation efficiency, as depicted in Figure 8c. CNC showed 3% degradation after 35 min of light irradiation. Pristine CaO degraded 10% of MBCF in 60 min. Increased photocatalytic activity was observed after doping CNC with CaO, with the maximal degradation rate of 18% achieved in 25−30 min. The extremely high % degradation was observed in a Ce/CNC-doped CaO specimen, indicating that the codoped nanomaterial was the most effective irradiation photocatalyst. The increase in photocatalytic activity of CaO, CNC, and Ce can be ascribed to a lower recombination rate of photo-induced charge carriers as a result of their doping. Electrons of VB excited to CB of induced Ce giving electron−hole pairs when codoped CaO was irradiated. Oxygen molecules (O_2) have been reduced by migrated charges into active oxygen radicals (O^*_2), while hydroxyl radicals were produced when holes in the VB of Ce reacted with water molecules.[60] Finally, produced O^*_2 and OH* radicals descended MBCF to generate degraded products. The degradation mechanism (redox reactions) is illustrated in eqs 2−6.

$$\text{CNC: Ce} - \text{CaO} + h\upsilon \rightarrow \text{CNC: Ce} - \text{CaO}(h^+ + e^-) \quad (2)$$

$$e^- + O_2 \rightarrow \bullet O_2^- \quad (3)$$

$$h^+ + OH^- \rightarrow \bullet OH \quad (4)$$

$$\bullet OH + \text{organic dye} \rightarrow \text{degradation products} \quad (5)$$

$$\bullet O_2^- + \text{organic dye} \rightarrow \text{degradation products} \quad (6)$$

In the above equations, the MBCF dye was degraded, and byproducts were produced. Usually, photocatalyst stability was examined by leaving completed activities uninterrupted for 3 days and obtaining an absorption spectrum from each sample every 24 h to record any variations in dye degradation. It has been determined that the dye has degraded every 24 h by spectrophotometry, and the findings are shown in Figure 8d. The CNC/Ce-doped CaO photocatalyst proved to be a promising performer and demonstrated outstanding stability. Table S1 compares the degradation of several dyes using various catalyst amounts and times. Metal oxide nanocomposites' photocatalytic activity was assessed by the reduction of MBCF under mercury lamp for a certain interval of time. The created holes in CNC (VB) and electrons transfer from the VB to CB of nanocomposites when illuminated under light. Subsequently, electrons transfer toward CB of CaO and holes move toward higher potential of CNC (VB), as shown in Figure 8e. Photogenerated electrons and holes play an important part in redox reactions when these interact with surrounding molecules in aqueous solution (Figure 8e).

In vitro microbicidal efficacy of pure and doped samples for pathogenic bacteria was studied by calculating inhibition zones through well diffusion assay are demonstrated in Table S2. The mechanism and obtained data of all samples showed

https://doi.org/10.1021/acsomega.2c02732
ACS Omega 2022, 7, 27503−27515

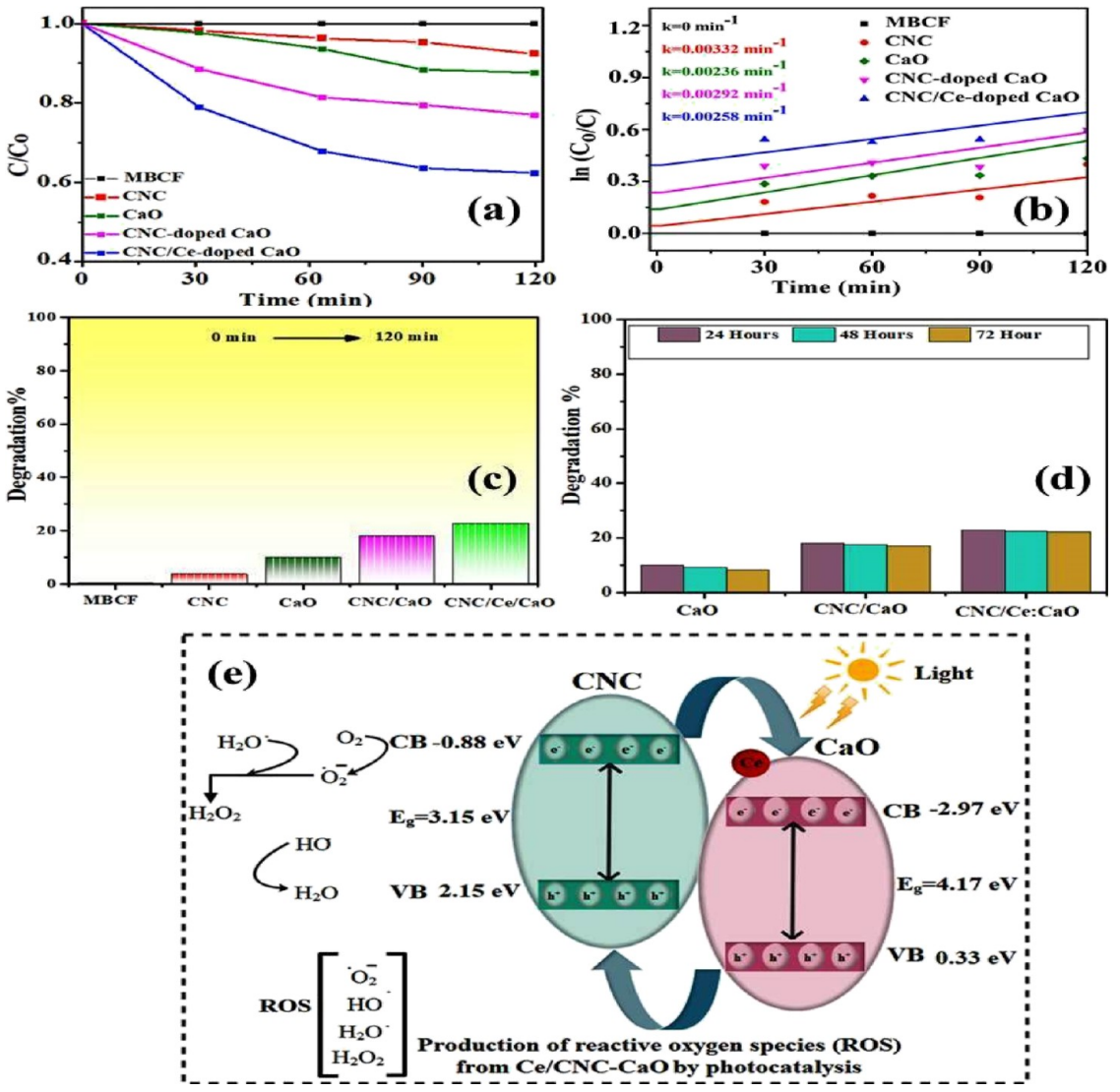

Figure 8. (a) C/C_0 vs time plot, (b) $\ln(C_0/C)$ vs time plot, (c) degradation % graph, (d) stability of codoped CaO samples, and (e) photoactivity mechanism of products.

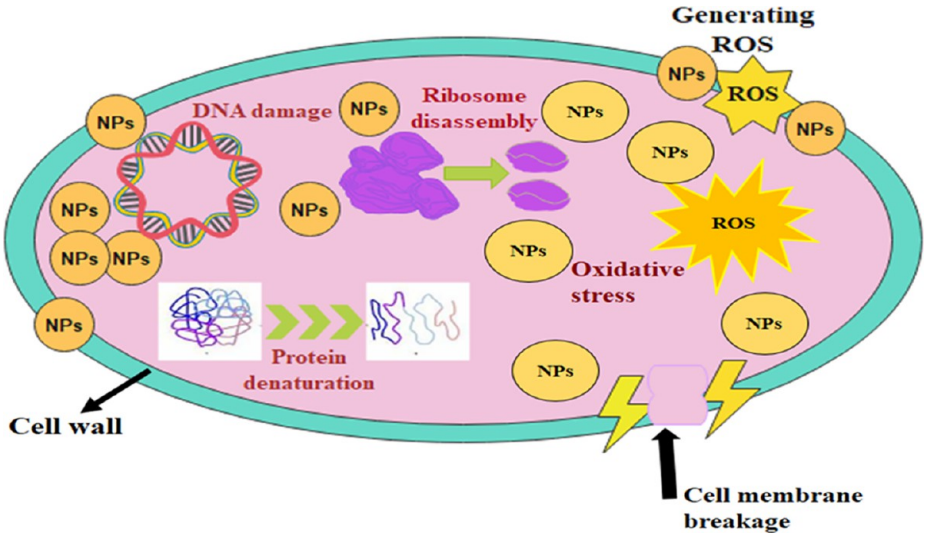

Figure 9. Schematic presentation of specimen's bactericidal mechanism.

https://doi.org/10.1021/acsomega.2c02732
ACS Omega 2022, 7, 27503−27515

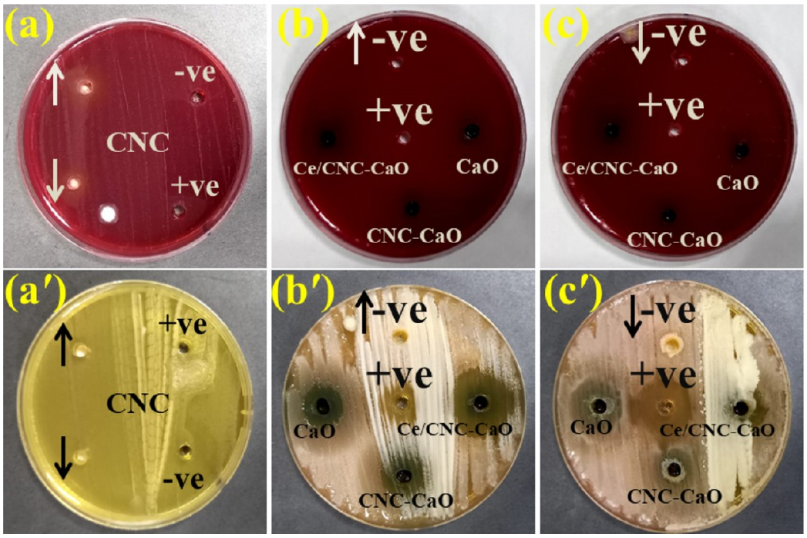

Figure 10. In vitro bactericidal efficacy of CNC (a), CaO, CNC-doped CaO, Ce/CNC-doped CaO (b,c) for *E. coli* and CNC (a′), CaO, CNC-doped CaO, Ce/CNC-doped CaO (b′,c′) for *S. aureus*.

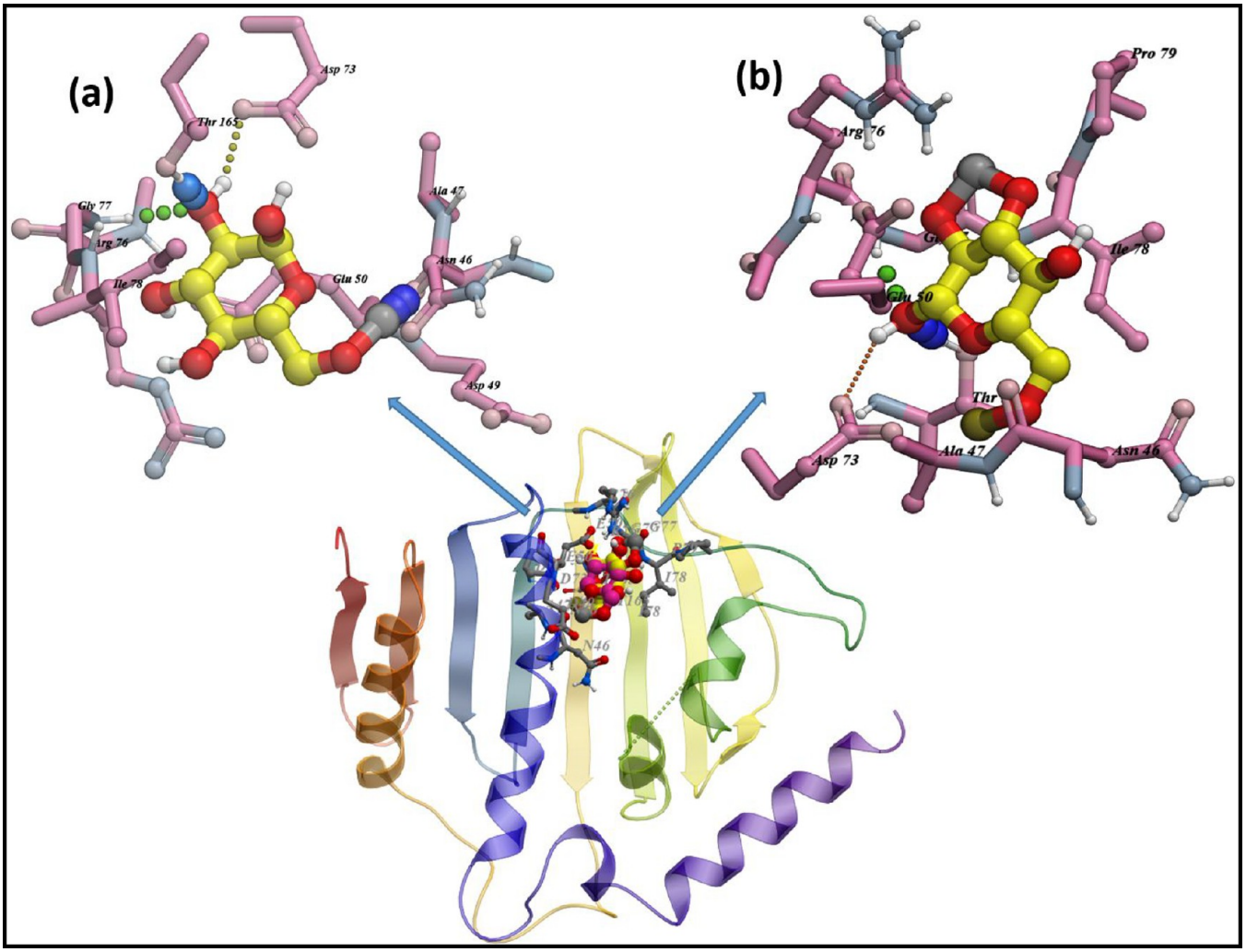

Figure 11. Binding interaction pattern of (a) CNC-doped CaO and (b) Ce/CNC-doped CaO nanocomposites with active site residues of DNA gyrase from *E. coli*.

antimicrobial activity against bacterial strains in Figures 9 and 10. A synergistic effect between the prepared samples and inhibition zones was depicted by results (Figure S1). In the case of CNC, significant bactericidal regions ($p < 0.05$) against

https://doi.org/10.1021/acsomega.2c02732
ACS Omega 2022, 7, 27503−27515

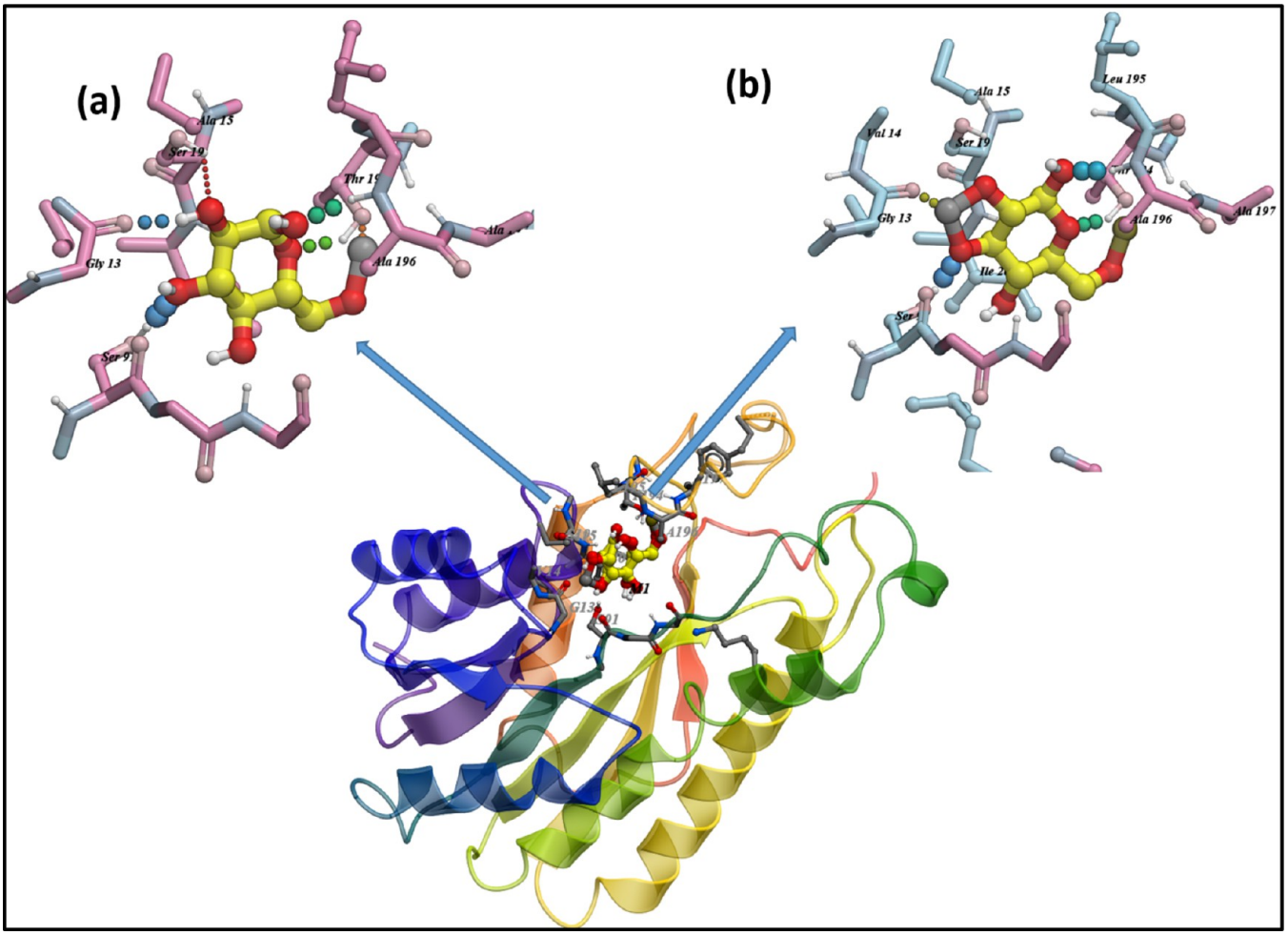

Figure 12. Binding interaction pattern of (a) CNC-doped CaO and (b) Ce/CNC-doped CaO nanocomposites with active site residues of FabI from *E. coli*.

Escherichia coli (3.30 and 4.45 mm) and *Staphylococcus aureus* (0.95 and 1.65 mm) were obtained at the minimum and maximum concentrations, correspondingly. Furthermore, pristine and codoped CaO inhibition areas against *Escherichia coli* ranged 1.90−7.15 mm and 3.30−7.15 mm while 1.90−7.80 mm and 2.25−7.80 mm for *Staphylococcus aureus* were recorded at minimum and maximum concentrations, respectively. These results were compared with those obtained with ciprofloxacin and DI water as 7.80 and 0 mm, correspondingly. Pristine and codoped CaO showed tremendous antimicrobial efficacy for Gram-positive in comparison with Gram-negative bacteria while CNC manifested intensified response vice versa. Codoped CaO efficiently highlighted bacteria-killing activity, as depicted in Table S2.

The effectiveness of antibacterial nanostructures is reliant on their size and concentration; therefore, oxidative stress of nanomaterials is also dependent on these parameters. Bacteria die as a result of the expulsion and bulging of cytoplasmic contents caused by reactive oxygen species (ROS), encasing their exterior membranes.[61] When cations substantially interact with the negative components of microbial cells, micro-microbes collapse as a result.[62,63] When cations interfere with bacterial ribosome activity and enzyme breakdown, micro-pathogens are unable to proliferate and sustain.[64]

In addition to their capacity to interact with bacterial cells and impair cell membrane permeability, metal-doped nanorods also have the potential to disrupt essential metabolic processes.[65] Nanorod toxicity to microbes is therefore studied in more detail. Antibiotics may be able to combat bacterial infections by inhibiting enzymes that play a critical role in bacterial survival, which is the primary virulence factor implicated in the infection.[66] Molecular docking experiments were carried out on DNA gyrase and FabI enzymes of *E. coli* as prospective targets based on the excellent bactericidal activity (in vitro) of CNC-doped CaO and Ce/CNC-doped CaO against *E. coli*.

The best docked conformation for CNC-doped CaO against DNA gyrase revealed H-bonding interaction with Gly77 (3.3 Å), Asn46 (1.3 Å), Asp73 (3.1 Å), and Thr165 (2.6 Å) having a binding score of −8.672 kcal/mol (Figure 11a). Similarly, the Ce/CNC-doped CaO nanocomposite showed a binding score of −9.174 kcal/mol having H-bonding interactions with Gly77 (3.1 Å), Asp73 (2.2 and 2.9 Å), and Thr165 (2.5 Å) alongside metal contact interactions with Arg76, as illustrated in Figure 11b.

In the case of FabI, the top-ranked docked complex for CNC-doped CaO revealed H-bonding interactions with Ser91 (2.7 Å), Gly13 (2.9 Å), Ser19 (2.9 Å), Thr194 (1.1 and 2.7 Å), and Ala196 (3.0 Å) having a binding score of −7.936 kcal/mol. On the other hand, Ce/CNC-doped CaO showed a binding score of −8.691 kcal/mol having H-bonding interactions with

https://doi.org/10.1021/acsomega.2c02732
ACS Omega 2022, 7, 27503−27515

Ser91 (3.0 Å), Gly13 (1.5 Å), Ser19 (3.1 Å), Thr194 (1.0 and 2.7 Å), and Ala196 (1.9 Å) as shown in Figure 12a, b.

4. CONCLUSIONS

Pristine and codoped CaO nanomaterial with Ce and CNC dopants were favorably synthesized via the sol−gel process. In the cubic structure of CaO, no obvious peak and dopant's crystal phase was observed in XRD spectra, which indicated that low concentrations of dopants in CaO are homogenously distributed. FTIR recorded all functional groups present in the sample. The presence of a typical absorption band around 874 cm^{-1} in the fingerprint region has been assigned to vibration modes of Ca−O−Ca bonding adsorption edge shifted toward higher wavelengths by the decrease in E_g from 4.17 to 3.41 eV upon Ce/CNC doping, which corresponds to the electronic characteristics of dopants. The PL spectra demonstrated the capabilities of nanoparticles by demonstrating better separation of charges and a reduction in the rate of e^-−h^+ recombination. Chemical composition was calculated with EDX, which confirmed the presence of constituent elements (e.g., Ca, O, and Na). A high degree of agglomeration and formation of nanorods of CaO upon doping could be observed using HR-TEM profiles while the d-spacing of pristine and doped CaO has been calculated as 0.326 and 0.250 nm, respectively. Upon the CNC/Ce incorporation, the degradation of the MBCF dye by CaO was enhanced under light irradiation. The highest photodegradation was recorded for codoped CaO, which showed synergistic effects under the visible source. CNC and Ce doping contents reduced the E_g width and decreased the charge carrier's recombination, which promoted the photoactivity. Pristine and codoped CaO showed tremendous antimicrobial efficacy against Gram-positive as compared to Gram-negative bacteria while CNC manifested intensified response vice versa. In silico MDS predicted the inhibition of DNA gyrase and FabI as the possible mechanism behind the biocidal activity of nanorods against bacterial strains.

■ ASSOCIATED CONTENT

Supporting Information

The Supporting Information is available free of charge at https://pubs.acs.org/doi/10.1021/acsomega.2c02732.

[1]Isolation and identification of *S. aureus* and *E. coli*;[2] antimicrobial activity;[3] molecular docking studies;[4] statistical analysis;[5] material characterization;[6] photocatalysis under dark conditions;[7] scavenging (DPPH) assay;[8] and effect of pH. Figures S1−S8, Tables S1 and S2 (PDF)

■ AUTHOR INFORMATION

Corresponding Authors

Muhammad Ikram − *Solar Cell Applications Research Lab, Department of Physics, Government College University Lahore, Lahore, Punjab 54000, Pakistan;* orcid.org/0000-0001-7741-789X; Email: dr.muhammadikram@gcu.edu.pk

Anwar Ul-Hamid − *Core Research Facilities, King Fahd University of Petroleum and Minerals, Dhahran 31261, Saudi Arabia;* orcid.org/0000-0002-0259-301X; Email: anwar@kfupm.edu.sa

Walid Nabgan − *Departament d'Enginyeria Química, Universitat Rovira i Virgili, 43007 Tarragona, Spain;* Email: walid.nabgan@urv.cat

Authors

Ayesha Khalid − *Physics Department, Lahore Garrison University Lahore, Lahore, Punjab 54000, Pakistan*

Anum Shahzadi − *Faculty of Pharmacy, The University of Lahore, Lahore, Punjab 54000, Pakistan*

Ali Haider − *Faculty of Veterinary and Animal Sciences, Muhammad Nawaz Shareef University Agriculture, Multan, Punjab 60000, Pakistan*

Sadia Naz − *Tianjin Institute of Industrial Biotechnology, Chinese Academy of Sciences, Tianjin 300308, China*

Misbah Naz − *Department of Chemistry, Division of Science and Technology, University of Education, Lahore, Punjab 54000, Pakistan*

Iram Shahzadi − *Punjab University College of Pharmacy, University of the Punjab, Lahore, Punjab 54000, Pakistan*

Junaid Haider − *Tianjin Institute of Industrial Biotechnology, Chinese Academy of Sciences, Tianjin 300308, China*

Alvina Rafiq Butt − *Physics Department, Lahore Garrison University Lahore, Lahore, Punjab 54000, Pakistan*

Complete contact information is available at: https://pubs.acs.org/10.1021/acsomega.2c02732

Notes

The authors declare no competing financial interest.

■ ACKNOWLEDGMENTS

We are exceedingly grateful for the assistance provided by the Higher Education Commission (HEC) through NRPU 20-17615.

■ REFERENCES

(1) Anwer, H.; Mahmood, A.; Lee, J.; Kim, K.; Park, J.; Yip, A. C. K. Photocatalysts for Degradation of Dyes in Industrial Effluents: Opportunities and Challenges. *Nano Res.* **2019**, *12*, 955−972.

(2) Kumar, R.; Umar, A.; Kumar, R.; Chauhan, M. S.; Kumar, G.; Chauhan, S. Spindle-like Co_3O_4-ZnO Nanocomposites Scaffold for Hydrazine Sensing and Photocatalytic Degradation of Rhodamine B Dye. *Eng. Sci.* **2021**, *16*, 288−300.

(3) Qiu, M.; Liu, L.; Ling, Q.; Cai, Y.; Yu, S.; Wang, S.; Fu, D.; Hu, B.; Wang, X. Biochar for the Removal of Contaminants from Soil and Water: A Review. *Biochar* **2022**, *4*, 1−25.

(4) Schwizer, F.; Okamoto, Y.; Heinisch, T.; Gu, Y.; Pellizzoni, M. M.; Lebrun, V.; Reuter, R.; Köhler, V.; Lewis, J. C.; Ward, T. R. Artificial Metalloenzymes: Reaction Scope and Optimization Strategies. *Chem. Rev.* **2018**, *118*, 142−231.

(5) Cheng, J.; Zhan, C.; Wu, J.; Cui, Z.; Si, J.; Wang, Q.; Peng, X.; Turng, L.-S. Highly Efficient Removal of Methylene Blue Dye froman Aqueous Solution Using Cellulose Acetate Nanofibrous Membranes by Polydopamine. *ACS Omega* **2020**, *5*, 5389.

(6) Aqeel, M.; Rashid, M.; Ikram, M.; Haider, A.; Naz, S.; Haider, J.; Ul-Hamid, A.; Shahzadi, A. Photocatalytic, Dye Degradation, and Bactericidal Behavior of Cu-Doped ZnO Nanorods and Their Molecular Docking Analysis. *Dalton Trans.* **2020**, *49*, 8314−8330.

(7) Yao, L.; Yang, H.; Chen, Z.; Qiu, M.; Hu, B.; Wang, X. Bismuth Oxychloride-Based Materials for the Removal of Organic Pollutants in Wastewater. *Chemosphere* **2021**, *273*, No. 128576.

(8) Nikazar, M.; Gorji, L. M.; Shojae, S.; Keynejad, K.; Haghighaty, A. H.; Jalili, F.; Mirzahosseini, A. R. H. Removal of Methyl Tertiary-Butyl Ether (MTBE) from Aqueous Solution Using Sunlight and Nano TiO_2. *Energy Sources, Part A* **2014**, *36*, 2305−2311.

(9) Xiong, S.; Yu, Y.; Wang, P.; Liu, M.; Chen, S.; Yin, X.; Wang, L.; Wang, H. Growth of AgBr/Ag3PO4 Heterojunction on Chitosan Fibers for Degrading Organic Pollutants. *Adv. Fiber Mater.* **2020**, *2*, 246−255.

(10) Deng, Y.; Zhao, R. Advanced Oxidation Processes (AOPs) in Wastewater Treatment. *Curr. Pollut. Rep.* **2015**, *1*, 167−176.
(11) Hao, M.; Qiu, M.; Yang, H.; Hu, B.; Wang, X. Recent Advances on Preparation and Environmental Applications of MOF-Derived Carbons in Catalysis. *Sci. Total Environ.* **2021**, *760*, No. 143333.
(12) An, T.; Yang, H.; Li, G.; Song, W.; Cooper, W. J.; Nie, X. Kinetics and Mechanism of Advanced Oxidation Processes (AOPs) in Degradation of Ciprofloxacin in Water. *Appl. Catal., B* **2010**, *94*, 288−294.
(13) Sun, Y.; Mwandeje, J. B.; Wangatia, L. M.; Zabihi, F.; Nedeljković, J.; Yang, S. Enhanced Photocatalytic Performance of Surface-Modified TiO2 Nanofibers with Rhodizonic Acid. *Adv. Fiber Mater.* **2020**, *2*, 118−122.
(14) Yu, C.; Yu, J. C.; Fan, C.; Wen, H.; Hu, S. Synthesis and Characterization of Pt/BiOI Nanoplate Catalyst with Enhanced Activity under Visible Light Irradiation. *Mater. Sci. Eng., B* **2010**, *166*, 213−219.
(15) Liu, X.; Ma, R.; Zhuang, L.; Hu, B.; Chen, J.; Liu, X.; Wang, X. Recent Developments of Doped G-C3N4 Photocatalysts for the Degradation of Organic Pollutants. *Crit. Rev. Environ. Sci. Technol.* **2021**, *51*, 751−790.
(16) Liu, N.; Jing, C.; Li, Z.; Huang, W.; Gao, B.; You, F.; Zhang, X. Effect of Synthesis Conditions on the Photocatalytic Degradation of Rhodamine B of MIL-53(Fe). *Mater. Lett.* **2019**, *237*, 92−95.
(17) Zhang, Y.; Shi, Z.; Shen, X.; Liu, J.; Duoerkun, G.; Shen, X.; Cao, W.; Liu, T.; Chen, Q.; Zhang, L. Construction of N-TiO_2/p-Ag_2O Junction on Carbon Fiber Cloth with Vis-NIR Photoresponse as a Filter-Membrane-Shaped Photocatalyst Photocatalysis View Project Construction of n-TiO_2/p-Ag_2O Junction on Carbon Fiber Cloth with Vis-NIR Photoresponse as a Filter-Membrane-Shaped Photocatalyst. *Adv. Fiber Mater.* **2020**, *2*, 13−23.
(18) Zou, J. P.; Wu, D. D.; Luo, J.; Xing, Q. J.; Luo, X. B.; Dong, W. H.; Luo, S. L.; Du, H. M.; Suib, S. L. A Strategy for One-Pot Conversion of Organic Pollutants into Useful Hydrocarbons through Coupling Photodegradation of MB with Photoreduction of CO2. *ACS Catal.* **2016**, *6*, 6861−6867.
(19) Jaiswal, K. K.; Dutta, S.; Pohrmen, C. B.; Verma, R.; Kumar, A.; Ramaswamy, A. P. Bio-Waste Chicken Eggshell-Derived Calcium Oxide for Photocatalytic Application in Methylene Blue Dye Degradation under Natural Sunlight Irradiation. *Inorg. Nano-Met. Chem.* **2020**, *51*, 1−10.
(20) Whited, R. C.; Flaten, C. J.; Walker, W. C. Exciton Thermoreflectance of MgO and CaO. *Solid State Commun.* **1973**, *13*, 1903−1905.
(21) Wang, H. J.; Cao, Y.; Wu, L. L.; Wu, S. S.; Raza, A.; Liu, N.; Wang, J. Y.; Miyazawa, T. ZnS-Based Dual Nano-Semiconductors (ZnS/PbS, ZnS/CdS or ZnS/Ag2S,): A Green Synthesis Route and Photocatalytic Comparison for Removing Organic Dyes. *J. Environ. Chem. Eng.* **2018**, *6*, 6771−6779.
(22) Butt, A. R.; Ejaz, S.; Baron, J. C.; Ikram, M.; Ali, S. CaO Nanoparticles as a Potential Drug Delivery Agent for Biomedical Applications. *Dig. J. Nanomater. Biostructures* **2015**, *10*, 799−809.
(23) Chen, A.; Ostrom, C. Palladium-Based Nanomaterials: Synthesis and Electrochemical Applications. *Chem. Rev.* **2015**, *115*, 11999−12044.
(24) Tu, K.; Wang, Q.; Lu, A.; Zhang, L. Nanoparticles and Graphene Oxide in Cellulose Matrix. *J. Phys. Chem. C* **2014**, *118*, 7202−7210.
(25) Lefatshe, K.; Muiva, C. M.; Kebaabetswe, L. P. Extraction of Nanocellulose and In-Situ Casting of ZnO/Cellulose Nanocomposite with Enhanced Photocatalytic and Antibacterial Activity. *Carbohydr. Polym.* **2017**, *164*, 301−308.
(26) Phung Hai, T. A.; Sugimoto, R. Photoluminescence Control of Cellulose via Surface Functionalization Using Oxidative Polymerization. *Biomacromolecules* **2017**, *18*, 4011−4021.
(27) Liu, S.; Zhang, L.; Zhou, J.; Xiang, J.; Sun, J.; Guan, J. Fiberlike Fe_2O_3 Macroporous Nanomaterials Fabricated by Calcinating Regenerate Cellulose Composite Fibers. *Chem. Mater.* **2008**, *20*, 3623−3628.
(28) Bahloul, A.; Kassab, Z.; El Bouchti, M.; Hannache, H.; Qaiss, A. E. K.; Oumam, M.; El Achaby, M. Micro- and Nano-Structures of Cellulose from Eggplant Plant (Solanum Melongena L) Agricultural Residue. *Carbohydr. Polym.* , *2021* (), 117311, DOI: 10.1016/j.carbpol.2020.117311.
(29) Gu, H.; Gao, C.; Zhou, X.; Du, A.; Naik, N.; Guo, Z. Nanocellulose Nanocomposite Aerogel towards Efficient Oil and Organic Solvent Adsorption. *Adv. Compos. Hybrid Mater.* **2021**, *4*, 459−468.
(30) Marwanto, M.; Maulana, M. I.; Febrianto, F.; Wistara, N. J.; Nikmatin, S.; Masruchin, N.; Zaini, L. H.; Lee, S.-H.; Kim, N.-H. Effect of Oxidation Time on the Properties of Cellulose Nanocrystals Prepared from Balsa and Kapok Fibers Using Ammonium Persulfate. *Polymers* **2021**, *13*, 1894.
(31) Yuan, B.; Li, L.; Murugadoss, V.; Vupputuri, S.; Wang, J.; Alikhani, N.; Guo, Z. Nanocellulose-Based Composite Materials for Wastewater Treatment and Waste-Oil Remediation. *ES Food Agrofor.* **2020**, *1*, 41−52.
(32) Santamaria-Echart, A.; Ugarte, L.; García-Astrain, C.; Arbelaiz, A.; Corcuera, M. A.; Eceiza, A. Cellulose Nanocrystals Reinforced Environmentally-Friendly Waterborne Polyurethane Nanocomposites. *Carbohydr. Polym.* **2016**, *151*, 1203−1209.
(33) Hui, Y.; Xie, W.; Gu, H. Reduced Graphene Oxide/Nanocellulose/Amino-Multiwalled Carbon Nanotubes Nanocomposite Aerogel for Excellent Oil Adsorption. *ES Food Agrofor.* **2021**, *5*, 38−44.
(34) Delogu, F.; Gorrasi, G.; Sorrentino, A. Fabrication of Polymer Nanocomposites via Ball Milling: Present Status and Future Perspectives. *Prog. Mater. Sci.* **2017**, *86*, 75−126.
(35) Fatima, A.; Yasir, S.; Ul-Islam, M.; Kamal, T.; Ahmad, M. W.; Abbas, Y.; Manan, S.; Ullah, M. W.; Yang, G. Ex Situ Development and Characterization of Green Antibacterial Bacterial Cellulose-Based Composites for Potential Biomedical Applications. *Adv. Compos. Hybrid Mater.* **2021**, *5*, 307−321.
(36) Pan, D.; Dong, J.; Yang, G.; Su, F.; Chang, B. B.; Liu, C.; Zhu, Y. C.; Guo, Z. Ice Template Method Assists in Obtaining Carbonized Cellulose/Boron Nitride Aerogel with 3D Spatial Network Structure to Enhance the Thermal Conductivity and Flame Retardancy of Epoxy-Based Composites. *Adv. Compos. Hybrid Mater.* **2021**, *5*, 58−70.
(37) Guo, Z.; Li, A.; Sun, Z.; Yan, Z.; Liu, H.; Qian, L. Negative Permittivity Behavior in Microwave Frequency from Cellulose-Derived Carbon Nanofibers. *Adv. Compos. Hybrid Mater.* **2022**, *5*, 50−57.
(38) Qu, K.; Sun, Z.; Shi, C.; Wang, W.; Xiao, L.; Tian, J.; Huang, Z.; Guo, Z. Dual-Acting Cellulose Nanocomposites Filled with Carbon Nanotubes and Zeolitic Imidazolate Framework-67 (ZIF-67)−Derived Polyhedral Porous Co3O4 for Symmetric Supercapacitors. *Adv. Compos. Hybrid Mater.* **2021**, *4*, 670−683.
(39) Barud, H. S.; Assunção, R. M. N.; Martines, M. A. U.; Dexpert-Ghys, J.; Marques, R. F. C.; Messaddeq, Y.; Ribeiro, S. J. L. Bacterial Cellulose-Silica Organic-Inorganic Hybrids. *J. Sol-Gel Sci. Technol.* **2008**, *46*, 363−367.
(40) Qi, G.; Liu, Y.; Chen, L.; Xie, P.; Pan, D.; Shi, Z.; Quan, B.; Zhong, Y.; Liu, C.; Fan, R.; Guo, Z. Lightweight Fe3C@Fe/C Nanocomposites Derived from Wasted Cornstalks with High-Efficiency Microwave Absorption and Ultrathin Thickness. *Adv. Compos. Hybrid Mater.* **2021**, *4*, 1226−1238.
(41) Junaid, M.; Imran, M.; Ikram, M.; Naz, M.; Aqeel, M.; Afzal, H.; Majeed, H.; Ali, S. The Study of Fe-Doped CdS Nanoparticle-Assisted Photocatalytic Degradation of Organic Dye in Wastewater. *Appl. Nanosci.* **2019**, *9*, 1593−1602.
(42) Touati, A.; Hammedi, T.; Najjar, W.; Ksibi, Z.; Sayadi, S. Photocatalytic Degradation of Textile Wastewater in Presence of Hydrogen Peroxide: Effect of Cerium Doping Titania. *J. Ind. Eng. Chem.* **2016**, *35*, 36−44.
(43) Lizundia, E.; Goikuria, U.; Vilas, J. L.; Cristofaro, F.; Bruni, G.; Fortunati, E.; Armentano, I.; Visai, L.; Torre, L. Metal Nanoparticles

Embedded in Cellulose Nanocrystal Based Films: Material Properties and Post-Use Analysis. *Biomacromolecules* **2018**, *19*, 2618−2628.
(44) Ramli, M.; Rossani, R. B.; Nadia, Y.; Banta Darmawan, T.; Febriani; Saiful; Ismail, Y. S. Nanoparticle Fabrication of Calcium Oxide (CaO) Mediated by the Extract of Red Dragon Fruit Peels (Hylocereus Polyrhizus) and Its Application as Inorganic-Anti-Microorganism Materials. *IOP Conf. Ser. Mater. Sci. Eng.* **2019**, *509*, No. 012090.
(45) Kodeh, F. S.; El-Nahhal, I. M.; Elkhair, E. A.; Darwish, A. H. Synthesis of CaO−Ag-NPs @CaCO3 Nanocomposite via Impregnation of Aqueous Sol Ag-NPs onto Calcined Calcium Oxalate. *Chem. Africa* **2020**, *3*, 679−686.
(46) Mirghiasi, Z.; Bakhtiari, F.; Darezereshki, E.; Esmaeilzadeh, E. Preparation and Characterization of CaO Nanoparticles from $Ca(OH)_2$ by Direct Thermal Decomposition Method. *J. Ind. Eng. Chem.* **2014**, *20*, 113−117.
(47) Mariano, M.; El Kissi, N.; Dufresne, A. Cellulose Nanomaterials: Size and Surface Influence on the Thermal and Rheological Behavior. *Polimeros* **2018**, *28*, 93−102.
(48) Anr, R.; Saleh, A. A.; Islam, M. S.; Hamdan, S.; Maleque, M. A. Biodiesel Production from Crude Jatropha Oil Using a Highly Active Heterogeneous Nanocatalyst by Optimizing Transesterification Reaction Parameters. *Energy Fuels* **2016**, *30*, 334−343.
(49) Nayebzadeh, H.; Saghatoleslami, N.; Tabasizadeh, M. Optimization of the Activity of KOH/Calcium Aluminate Nanocatalyst for Biodiesel Production Using Response Surface Methodology. *J. Taiwan Inst. Chem. Eng.* **2016**, *68*, 379−386.
(50) Arularasu, M. V.; Harb, M.; Sundaram, R. Synthesis and Characterization of Cellulose/TiO2 Nanocomposite: Evaluation of in Vitro Antibacterial and in Silico Molecular Docking Studies. *Carbohydr. Polym.* **2020**, *249*, No. 116868.
(51) Schiebel, J.; Chang, A.; Shah, S.; Lu, Y.; Liu, L.; Pan, P.; Hirschbeck, M. W.; Tareilus, M.; Eltschkner, S.; Yu, W.; Cummings, J. E.; Knudson, S. E.; Bommineni, G. R.; Walker, S. G.; Slayden, R. A.; Sotriffer, C. A.; Tonge, P. J.; Kisker, C. Rational Design of Broad Spectrum Antibacterial Activity Based on a Clinically Relevant Enoyl-Acyl Carrier Protein (ACP) Reductase Inhibitor. *J. Biol. Chem.* **2014**, *289*, 15987−16005.
(52) Bharti, B.; Li, H.; Liu, D.; Kumar, H.; Manikandan, V.; Zha, X.; Ouyang, F. Efficient Zr-Doped FS−TiO_2/SiO_2 Photocatalyst and Its Performance in Acrylonitrile Removal under Simulated Sunlight. *Appl. Phys. A: Mater. Sci. Process.* **2020**, *126*, 1−10.
(53) Nakamura, M.; Mitsuhashi, H.; Takezawa, N. Oxygen Species Formed on Different Surface Sites of CaO by Decomposition of N2O and the Reactivity. *J. Catal.* **1992**, *138*, 686−693.
(54) Sinha, S.; Aman, A. K.; Singh, R. K.; Kr, N.; Shivani, K. Calcium Oxide(CaO) Nanomaterial (Kukutanda Twak Bhasma) from Egg Shell: Green Synthesis Physical Properties and Antimicrobial Behaviour. *Mater. Today Proc.* **2020**, *43*, 3414−3419.
(55) An, B.; Ryu, K. H.; Kim, Y. R.; Lee, S. H. Activation of Methane to C2 Hydrocarbons over Unpromoted Calcium Oxide Catalysts. *Bull. Korean Chem. Soc.* **2007**, *28*, 1049−1052.
(56) Satsuma, A.; Akahori, R.; Kato, M.; Komai, S. I.; Yoshida, H.; Hattori, T. Structure-Sensitive Reaction over Calcium Oxide - Decomposition of Nitrous Oxide. *J. Mol. Catal. A: Chem.* **2000**, *155*, 81−88.
(57) Liu, J.; Liu, M.; Chen, S.; Wang, B.; Chen, J.; Yang, D. P.; Zhang, S.; Du, W. Conversion of Au(III)-Polluted Waste Eggshell into Functional CaO/Au Nanocatalyst for Biodiesel Production. *Green Energy Environ.* **2021**, *7*, 019.
(58) Widyawati, M.; Church, T. L.; Florin, N. H.; Harris, A. T. Hydrogen Synthesis from Biomass Pyrolysis with in Situ Carbon Dioxide Capture Using Calcium Oxide. *Int. J. Hydrogen Energy* **2011**, *36*, 4800−4813.
(59) Lu, H.; Smirniotis, P. G. Calcium Oxide Doped Sorbents for CO_2 Uptake in the Presence of SO_2 at High Temperatures. *Ind. Eng. Chem. Res.* **2009**, *48*, 5454−5459.
(60) Sharma, S.; Bhattacharya, A. Drinking Water Contamination and Treatment Techniques. *Appl. Water Sci.* **2017**, *7*, 1043−1067.
(61) Ikram, M.; Tabassum, R.; Qumar, U.; Ali, S.; Ul-Hamid, A.; Haider, A.; Raza, A.; Imran, M.; Ali, S. Promising Performance of Chemically Exfoliated Zr-Doped MoS2nanosheets for Catalytic and Antibacterial Applications. *RSC Adv.* **2020**, *10*, 20559−20571.
(62) Altaf, S.; Haider, A.; Naz, S.; Ul-Hamid, A.; Haider, J.; Imran, M.; Shahzadi, A.; Naz, M.; Ajaz, H.; Ikram, M. Comparative Study of Selenides and Tellurides of Transition Metals (Nb and Ta) with Respect to Its Catalytic, Antimicrobial, and Molecular Docking Performance. *Nanoscale Res. Lett.* **2020**, *15*, 1.
(63) Guimarães, A. C.; Meireles, L. M.; Lemos, M. F.; Guimarães, M. C. C.; Endringer, D. C.; Fronza, M.; Scherer, R. Antibacterial Activity of Terpenes and Terpenoids Present in Essential Oils. *Molecules* **2019**, *24*, 2471.
(64) Iyyappa Rajan, P.; Judith Vijaya, J.; Jesudoss, S. K.; Kaviyarasu, K.; John Kennedy, L.; Jothiramalingam, R.; Al-Lohedan, H. A.; Vaali-Mohammed, M. A. Green-Fuel-Mediated Synthesis of Self-Assembled NiO Nano-Sticks for Dual Applications-Photocatalytic Activity on Rose Bengal Dye and Antimicrobial Action on Bacterial Strains. *Mater. Res. Express* **2017**, *4*, No. 085030.
(65) Thill, A.; Zeyons, O.; Spalla, O.; Chauvat, F.; Rose, J.; Auffan, M.; Flank, A. M. Cytotoxicity of CeO_2 Nanoparticles for Escherichia Coli. Physico-Chemical Insight of the Cytotoxicity Mechanism. *Environ. Sci. Technol.* **2006**, *40*, 6151−6156.
(66) Konieczna, I.; Zarnowiec, P.; Kwinkowski, M.; Kolesinska, B.; Fraczyk, J.; Kaminski, Z.; Kaca, W. Bacterial Urease and Its Role in Long-Lasting Human Diseases. *Curr. Protein Pept. Sci.* **2013**, *13*, 789−806.

https://doi.org/10.1021/acsomega.2c02732
ACS Omega 2022, 7, 27503−27515